ACS Catalysis

pubs.acs.org/acscatalysis Research Article

Mechanisms and Kinetics of the Dehydrogenation of C_6-C_8 Cycloalkanes, Cycloalkenes, and Cyclodienes to Aromatics in H-MFI Zeolite Framework

Hansel Montalvo-Castro, Mykela DeLuca, Lauren Kilburn, and David Hibbitts*

Cite This: *ACS Catal.* 2023, 13, 99–112 Read Online

ABSTRACT: This work employs periodic density functional theory to elucidate dehydrogenation mechanisms of C_6-C_8 cycloalkanes, cycloalkenes, and cyclodienes into aromatics during methanol-to-olefin (MTO) chemistries in H-MFI zeolites. Aromatic compounds act as co-catalysts that predominantly form ethylene over propylene products and lead to site-blocking polyaromatic compounds; thus, understanding the formation of aromatic compounds during MTO is critical to understanding its selectivity and catalyst stability. Ring dehydrogenation reactions occur via sequential hydride transfer followed by deprotonation. The rate-controlling hydride transfer reactions were investigated with surface-bound protons (Z−H) and alkyls ($Z-C_nH_{2n+1}$) as hydride-accepting species. Hydride transfers via proton-mediated routes occur with intrinsic free energy barriers (623 K) of 215 kJ mol^{-1} for C_6H_{12}, 164 kJ mol^{-1} for C_6H_{10}, and 141 kJ mol^{-1} for C_6H_8, whereas methyl-mediated counterparts occur with intrinsic free barriers of 101, 95, and 81 kJ mol^{-1}, respectively. Transition states for hydride transfer reactions prefer channel intersections within MFI networks, and their activation barriers suggest that methyl-mediated routes are favored over proton-mediated counterparts during MTO. Methyl substituents on hydrocarbon rings generally increase activation barriers for hydride transfers that occur proximal to the $-CH_3$, partly because of steric hindrances between the hydride acceptor and ring-bound $-CH_3$. Rapid double-bond isomerization within cyclohexenes and cyclohexadienes allows hydride transfer reactions to occur away from sterically hindering methyl substituents in methylated and dimethylated C_6 ring hydrocarbons. The impact of carbocation substitution in hydride-accepting species was explored by contrasting barriers of methyl ($Z-CH_3$), ethyl ($Z-C_2H_5$), 2-propyl ($Z-C_3H_7$), and *tert*-butyl ($Z-C_4H_9$) surface-bound alkyls. Intrinsic activation barriers decrease with increasing substitution of the alkyl hydride acceptor, consistent with those alkyls forming more stable carbocations. However, when accounting for steric hindrances associated with the co-adsorption of hydrocarbon rings near surface-bound alkyls, apparent free barriers are larger for more-substituted alkyls. Taking these apparent barriers into account, we predict that methyl-mediated hydride transfer reactions are responsible for the aromatization of hydrocarbon rings during MTO, leading to the CH_4 formed during MTO reactions as the aromatic pool is enriched.

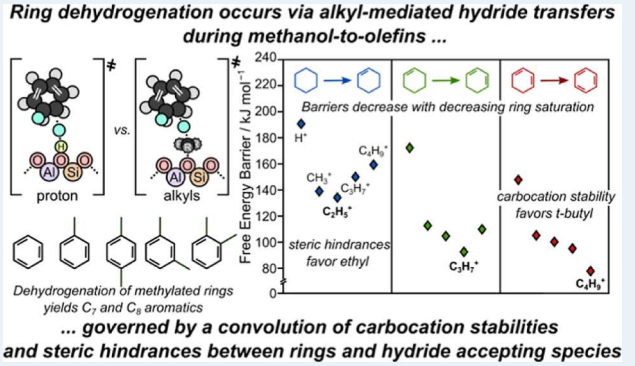

KEYWORDS: *methanol-to-hydrocarbons, cyclization, dehydrogenation, hydride transfer, zeolites, aromatics, carbocation, sterics*

1. INTRODUCTION

Olefins are the preferred chemical building blocks to produce many consumer goods, and their demand is mainly supplied from the steam cracking of naphthenes and alkane gas mixtures. Alternative strategies for their production include methanol-to-olefin (MTO) chemistries in proton-form zeolites. MTO reactions proceed via a hydrocarbon pool mechanism where two catalytic cycles—olefin-based and aromatic-based[1−6]—cooperate to form C_2-C_4 alkenes (Scheme 1).[1,7−14] Methylating agents such as methanol (CH_3OH, MeOH) and dimethyl ether (CH_3OCH_3, DME) methylate zeolite surfaces, olefins, and aromatics in pathways that lead—directly or indirectly—to the observed products. For example, olefins can grow by subsequent methylation reactions until they reach sizes capable of cracking (C_{6+}) to form $C_{\geq 3}$ alkenes. These alkenes, in turn, may either diffuse from the zeolite as gas-phase products or reincorporate into the olefin-based cycle.[2,6,15,16] Alternatively, alkenes may react with other alkenes or methanol (via formaldehyde-assisted routes) to form alkanes and dienes.[17−19] Dienes can cyclize to

Received: July 12, 2022
Revised: November 7, 2022
Published: December 12, 2022

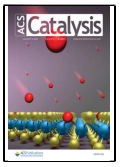

https://doi.org/10.1021/acscatal.2c03360
ACS Catal. 2023, 13, 99−112

Scheme 1. Olefin-Based (Blue) and Aromatic-Based (Red) Cycles of Methanol-to-Olefin Chemistries[a]

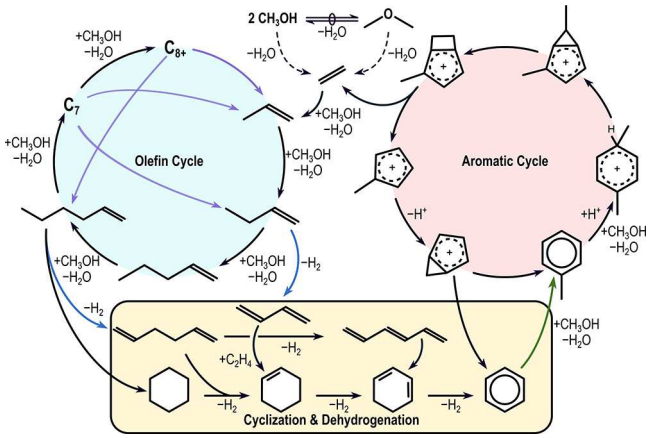

[a]Cyclization and dehydrogenation (yellow) events connect the two cycles. Blue arrows indicate dehydrogenation reactions to form dienes, the green arrow indicates an arene methylation event, and purple arrows indicate cracking from large olefins into their smaller counterparts.

cycloalkenes and subsequently dehydrogenate to form aromatic compounds,[20−22] which can cocatalyze the formation of olefins through isomerization and dealkylation reactions in the aromatic cycle.[1,7,16,23,24] Additional cyclization reactions may occur between dienes and aromatics to form polyaromatic compounds that cause catalyst deactivation by blocking sites and diffusion pathways.[25−29] Hence, elucidating specific pathways that form aromatic compounds is crucial to understanding the relative propagation of the olefin- and aromatic-based cycles and catalyst deactivation.

The formation of aromatic species during MTO chemistries follows the formation of dienes, which are precursors to cyclization events.[20−22,30,31] Dienes can be formed from olefin-mediated and formaldehyde-mediated (CH_2O) hydride transfers but typically proceed by CH_2O-mediated routes at MTO conditions as evidenced by (1) the detection of dienes during co-reaction of CH_2O with alkenes[32−38] and (2) lower density functional theory (DFT)-predicted barriers for diene formation via CH_2O-mediated routes compared to alkene-mediated routes.[39−42] Furthermore, co-feeding CH_2O during MTO chemistries results in higher selectivity toward dienes, aromatics, and ethylene with concurrent decreases in catalyst lifetimes.[18,30,43] For example, cofeeding CH_2O with methanol (H-ZSM-5, Si/Al = 90, 171 mbar MeOH, 9 mbar CH_2O, and 60 mbar H_2O at 750 K) increases the selectivity toward dienes (0.7% vs 0.4% with pure MeOH) and aromatics (12.2% vs 2.4% with pure MeOH) with only slight changes in alkane selectivity (3.1% vs 2.8% with pure MeOH), suggesting that the observed increases of diene and aromatic selectivity are a result of direct reaction between alkenes and CH_2O.

Fast scrambling of methanol with ^{13}C-labeled CH_2O disallows isotopic tracking of $^{13}CH_2O$, as suggested from similar ^{13}C fraction across all MTO products. However, co-feeding 1-butene with $^{13}CH_2O$ and $^{12}CH_3OH$ lowers the extent of scrambling reactions, allowing for $^{13}CH_2O$ tracing. This work showed the highest ^{13}C content in dienes (10.5% butadiene, 7.4% pentadiene), aromatics (11.6% xylene, 10.3% trimethylbenzene), and ethylene (4.7%; highest among all alkenes).[5] These results suggest that CH_2O co-feeds transform into dienes, aromatics, and ultimately ethylene through the aromatic-based cycles. These shifts in the relative rates of these two cycles can also be observed by co-feeding small concentrations of aromatics with methanol on H-ZSM-5.[5]

The role of formaldehyde and dienes in the formation of aromatic species is also supported by previous studies on catalyst lifetimes. Co-feeding H_2 during MTO chemistries enhances catalyst lifetimes for a variety of topological frameworks, including CHA and MFI.[44,45] This is likely because H_2 selective decreases the concentration of hydrogen poor compounds (such as formaldehyde and dienes) via hydrogenation reactions,[45,46] limiting the formation of aromatics and thus the propagation of aromatic-based cycle as measured by a decrease in ethene-to-propene ratios within H-ZSM5.[44,45] This is supported by theoretical work that suggests apparent barriers of butadiene, hexadiene, and formaldehyde are 10−30 kJ mol^{-1} lower than those of C_2−C_4 alkenes in both MFI and CHA.[47] CH_2O co-feeds in the presence of CH_2O-scavenging Y_2O_3 species during MTO reduce deactivation rates in CHA,[48] which—as an alternative method to reduce formaldehyde concentrations—further indicates that formaldehyde facilitates aromatic formation and thus enhances deactivation. These observations are rationalized by DFT calculations demonstrating that at conditions relevant to MTO, dienes are predominantly formed via CH_2O-assisted routes over alkene disproportionation routes, implying that formaldehyde influences aromatic formation as a precursor to the formation of dienes.[39]

Cyclization events during MTO chemistries (Scheme 1, yellow) have been proposed to occur via (1) direct cyclization of unsaturated compounds,[20−22,49,50] (2) Diels−Alder cycloaddition reactions,[51−54] and (3) formaldehyde-mediated routes[55,56] via the formation of polyene alcohols, which undergo dehydrocyclization into diene rings—each of which can form C_6 rings of varying saturation. DFT calculations on direct cyclization of 1,5-hexadiene on bare and embedded cluster (single T12-site) models suggest that C_5 and C_6 hydrocarbon rings may form from secondary and primary surface-bound dienes, respectively.[21] These studies were extended to C_7 and C_8 diene precursors, and it was found that the activation barriers for 1,6-cyclization routes trend opposite with degree of methylation C_6 > C_7 > C_8,[22] suggesting that cyclization pathways may also form methylated hydrocarbon rings such as methylcyclohexene and dimethylcyclohexene. Experimental investigations have shown that trienes can also lead to the formation of cyclic hydrocarbons (e.g., cyclohexadiene) and that cyclization is exothermic and irreversible.[50,57−61] Diels−Alder reactions, similarly, could lead to the formation of cyclic species from reactions of dienes and alkenes, although these have only been studied on non-acidic zeolites as the reaction is typically not associated with Brønsted acid sites.[62−65] Alternatively, dehydrative reactions of dienes with formaldehyde can result in the formation of cyclopentadiene (C_5H_6) via 1,3-butadien-1-ol as an intermediate. C_5H_6 has been identified during MTO[66,67] and has been proposed to be a precursor to deactivation either by interacting with aromatics[68] or by undergoing alkylation, isomerization, and hydride transfers that yield deactivating species,[66,69,70] potentially via C_6 intermediates. In summary, all cyclization pathways can lead, directly or indirectly, to the formation of six-member ring compounds with varying degrees of saturation—but do not directly lead to aromatic compounds.

https://doi.org/10.1021/acscatal.2c03360
ACS Catal. 2023, 13, 99−112

Hydrocarbon rings must undergo dehydrogenation upon formation to form aromatics.[71] The specific pathways that govern the dehydrogenation of hydrocarbon rings, however, are still to be elucidated. This work employs DFT to explore dehydrogenative aromatization of C_6−C_8 cycloalkanes, cycloalkenes, and cyclodienes in the MFI (ZSM-5) framework. Dehydrogenation occurs through hydride transfer reactions between cyclic hydrocarbons and surface-bound alkyl species formed by the demethylation of reactant methanol and DME (methyls) or protonation of product alkenes (e.g., to form ethyl). The extent of surface alkyl involvement depends on their relative surface concentrations and thus the conversion and time on stream. Hydride transfer barriers are lower in the MFI channel intersections than in the straight channel, reflecting transition states that are too large (7−10 C atoms in the reactions studied here) to be effectively solvated by the smaller MFI straight channels. Methyl substituents on the rings generally increase barriers for hydride transfer reactions occurring at proximal positions, while C=C double bonds generally decrease barriers for nearby hydride transfer reactions. The dehydrogenation of C_7−C_8 hydrocarbon rings, however, is thermodynamically favored from double-bond isomerization events among cyclohexenes and cyclohexadienes. Finally, substituted alkyls are better hydride acceptors than unsubstituted alkyls, suggesting that reaction barriers are governed by the relative stability of carbocations derived from these surface alkyls.

2. METHODS

Periodic DFT calculations were performed using the Vienna ab initio simulation package[72−75] in a fully periodic MFI unit cell, as implemented in the computational catalysis interface.[76] Plane-wave basis sets were constructed with the projector augmented wave potentials with an energy cutoff of 400 eV. The exchange and correlation energies were estimated with the Perdew−Burke−Ernzerhof (PBE) form of the generalized gradient approximation.[77−79] The DFT-D3 method with Becke and Johnson (D3BJ) damping corrected for dispersive interactions.[80−82]

Gas calculations were performed in a 15 Å × 15 Å × 15 Å vacuum unit cell. Gas calculations involving charged species (e.g., carbocation formation energies; see SectionS5 in the Supporting Information) were performed with a uniform compensating background charge with dipole and quadrupole corrections. Structures with unpaired electrons were optimized spin polarized.

The MFI-zeolite structure was obtained from the experimental results of van Koningsveld[83] to minimize restructuring artifacts that may influence energy estimates.[84] The T- and O-site indices referenced in this work follow the international zeolite association convention.[85] The shape and lattice parameters for MFI (a = 20.090 Å, b = 19.738 Å, and c = 13.142 Å) were fixed across all calculations. All calculations were performed at T11, to provide access to the straight channel and the channel intersection. Previous work suggests that surface methylation (a key elementary reaction within the context of this work) occurs with lower activation barriers at T11 relative to T3, T10, and T12 in MFI.[86] Moreover, recent work exploring the Al location within MFI suggests that T11 is among the most favorable Al site locations,[87] thus justifying its selection for modeling in this work.

Structures were optimized in a two-step procedure, which is more efficient than traditional single-step optimizations.[76] In the first step, structures were electronically converged so that energies varied by $<10^{-4}$ eV between iterations, and the maximum force on each atom was <0.05 eV Å^{-1}. In the second step, structures were further optimized so that energies varied by $<10^{-6}$ eV between iterations, and the maximum force on each atom was <0.05 eV Å^{-1}. Forces for the first and second steps were computed using a fast Fourier transform grid with cutoffs of 1.5-times and 2.0-times of the plane-wave cutoff, respectively. The Brillouin Zone was sampled at the Γ-point.[88]

Transition state searches were initiated using the nudged elastic band method (NEB),[89] with 16 images along the reaction coordinate. NEBs were converged so that the maximum force across all atoms in all images was <0.5 eV Å^{-1}. Following NEB convergence, transition state structures were isolated using the Dimer method[90] and optimized until the maximum force on all atoms was <0.05 eV Å^{-1}. Dimer calculations were also performed using a two-step method analogous to that described for optimizations.

Vibrational frequencies for reactant, product, and transition states were calculated by using a fixed displacement method in which all adsorbate atoms (including protons), the framework Al atom, and the four O atoms attached to the Al atom were displaced. Vibrational frequencies are used to estimate zero-point vibrational energy and temperature-corrected free energies (G) and enthalpies (H) for all states (more details provided in Section S1 in the Supporting Information). Similar to previous works,[39,47,86,91] vibrational modes <60 cm^{-1} were replaced with 60 cm^{-1} (except for imaginary modes along the reaction coordinate in transition states) as these low-frequency modes—traditionally associated with frustrated or hindered motions—are inaccurate and significantly contribute to vibrational entropy estimates.

There are four O atoms surrounding T11: O14, O16, O24, and O25. Previous work shows that O24 is inaccessible by reactants of interest in this work[92]—hence, O24 was not considered here, while the other three O atoms were examined for all steps. Zeolite-catalyzed reactions are influenced by the different shapes and sizes of the confining voids near catalytic active sites. All adsorbate and transition state calculations were therefore examined in both the straight channel and intersection environments. The aim of this work is to identify the trends that govern cyclic dehydrogenation reactions, and DFT-D3 level theory is sufficient to describe such trends while avoiding the computational expense of more physically accurate AIMD or higher-level calculations (e.g., MP2). One-off static DFT calculations, however, do not sufficiently probe the potential energy surface of reactant, product, or transition states; as such, all reactant, product, and transition states were systematically reoriented based on their relevant interactions with the zeolite framework, explained in detail in our prior work,[92] followed by the aforementioned two-step optimization procedure. Systematic reorientations increase the likelihood of identifying the global energy minima and the lowest-energy saddle-point connecting those minima. Previous work shows that systematic reorientations can lower DFT estimated energies by ∼10−50 kJ mol^{-1}.[92] These differences are significant as they may either include irrelevant pathways or exclude relevant ones; hence, systematic reorientations (enhanced sampling) improve the accuracy of DFT calculated energies while being ∼100 times more computationally efficient than AIMD simulations or alternative global minimization strategies while also being applicable to transition state searches.

https://doi.org/10.1021/acscatal.2c03360
ACS Catal. 2023, 13, 99−112

3. RESULTS AND DISCUSSION

3.1. Contrasting Proton- and Methyl-Mediated Dehydrogenation of C_6 Hydrocarbon Rings in MFI.

The dehydrogenation of a cyclic hydrocarbon by hydride transfer may proceed via a proton-mediated pathway (Scheme 2, inner) to form H_2 and a carbocation

$$C_6H_m + Z - H \rightarrow C_6H_{m-1}^+ + Z^- + H_2(g) \quad (1)$$

where m is 12 for cyclohexane, 10 for cyclohexene, and 8 for cyclohexadiene, and Z is the zeolite framework (including the O atom to which the proton binds). The $C_6H_{m-1}^+$ carbocation will then deprotonate to restore the Brønsted acid site

$$C_6H_{m-1}^+ + Z^- \rightarrow C_6H_{m-2} + Z - H \quad (2)$$

Carbocation ring deprotonation occurs with activation free energies (ΔG_{act}) < 15 kJ mol^{-1}, suggesting that this step is kinetically irrelevant. This is consistent with experimental work showing rapid double-bond isomerization and equilibrium among double-bond isomers for alkenes at conditions similar to MTO;[93,94] as such, protonation and deprotonation will be assumed facile in the remainder of this work.

Surface methylation reaction occurs readily at high temperatures (>623 K)[95−98]

$$ROCH_3(g) + Z - H \rightarrow ROH(g) + Z - CH_3 \quad (3)$$

where R is H or CH_3 for methanol and DME as methylating agents, respectively. These surface-bound methyls can react with hydrocarbon rings in hydride transfer reactions via a methyl-mediated pathway (Scheme 2, outer)

$$C_6H_m + Z - CH_3 \rightarrow C_6H_{m-1}^+ + Z^- + CH_4(g) \quad (4)$$

Scheme 2. Sequential Routes for Proton-Mediated Dehydrogenation (Inner Cycle) and Methyl-Mediated Dehydrogenation (Outer Cycle)[a]

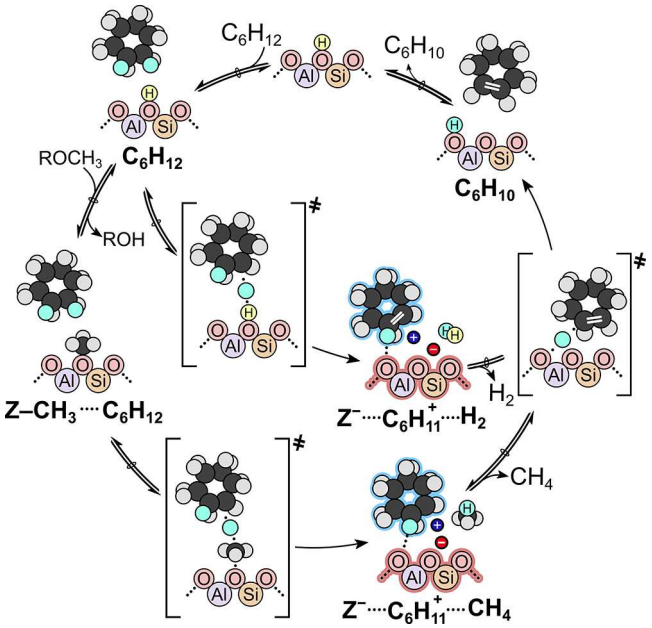

[a]The relevant transition states (i.e., the hydride transfers) for each route are indicated with single-directed arrows.

followed by deprotonation of $C_6H_{m-1}^+$ as shown in Eq 2. Here, we compare proton-mediated and methyl-mediated dehydrogenation routes for cyclohexane (C_6H_{12}), cyclohexene (C_6H_{10}), and cyclohexadiene (C_6H_8).

During MTO conditions, protons and surface-bound alkyls are expected to readily transfer between O atoms at a given T-site; as such, all reactions in this work were investigated at the three accessible O atoms of T-11 (O14, O16, and O25), and activation energies, ΔG_{act} (623 K), of proton-mediated and methyl-mediated hydride transfers are reported in Figure 1.

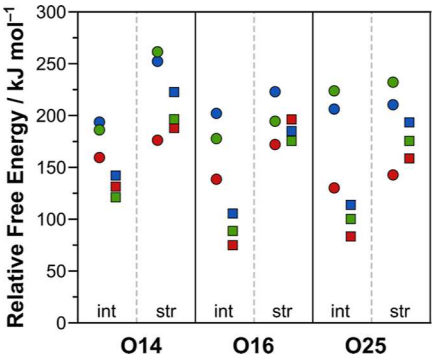

Figure 1. Free energy barriers as a function of T-site oxygen zeolite environment for C_6H_{12} (blue), C_6H_{10} (green), and C_6H_8 (red) dehydrogenations via proton- (circles) and methyl-mediated (squares) pathways. Free energy values are reported at 623 K and relative to the best overall reactant state, respectively. Enthalpy (H), entropy (S), and free energy (G) values are reported in Table S1 in the Supporting Information with corresponding structures shown in Figures S10−S15.

Additionally, transition states were investigated in both the straight channel and the channel intersection to probe different local confinements, also reported in Figure 1. Comparing O atoms, ΔG_{act} values are generally comparable for transition states interacting with O16 and O25, because both O sites have similar environments. The barriers at O14 are, on average, higher than those at O16 and O25 because O14 resides primarily in the straight channel with limited access to the channel intersection. Dehydrogenation reactions occur more favorably in channel intersections than in straight channels for all examined pathways and reacting species at each of the three examined oxygens. This suggests that the smaller straight channel environment imposes steric constraints on bulkier transition states and makes these transition states less favorable. Moreover, the preference for the MFI intersection is greater for bulkier methyl-mediated transition states than for proton-mediated transition states. This is consistent with prior studies of arene methylation reactions,[92] where activation barriers for surface methylation reactions (a relatively small transition state) were found to be lower when transition states were in the straight channel, whereas transition states for arene methylation—which involves a bulkier reagent—occur more favorably in intersections. This preference for reactions to occur in channel intersections is seen throughout this work.

Free energy barriers (relative to the ring adsorbed near the surface-bound methyl or proton, 623 K) are 114, 69, and 60 kJ mol^{-1} lower for methyl-mediated hydride transfer reactions than for proton-mediated hydride transfer reactions with cyclohexane, cyclohexene, and cyclohexadiene, respectively (Figure 2a−c). These barrier differences can be rationalized from structural inspection of the corresponding transition

https://doi.org/10.1021/acscatal.2c03360
ACS Catal. 2023, 13, 99−112

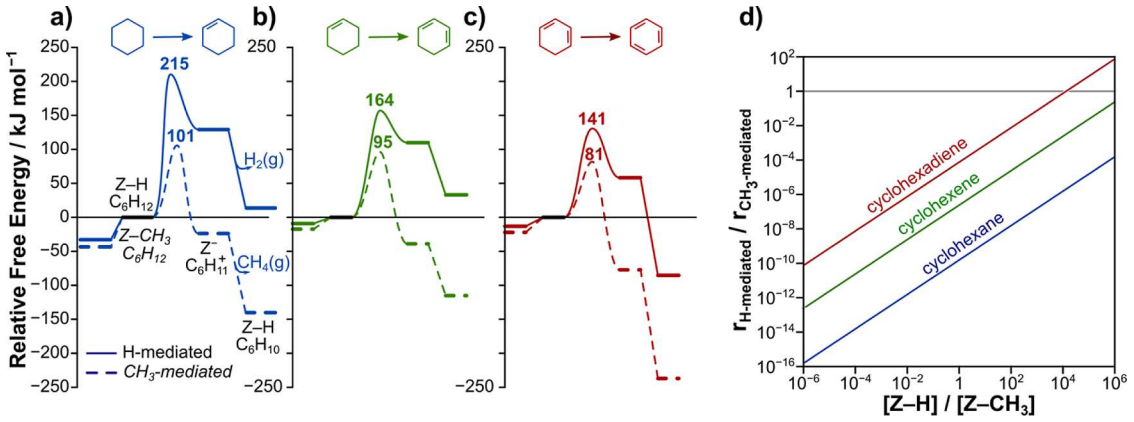

Figure 2. Reaction coordinate diagram for proton- (solid) and methyl-mediated (dashed) dehydrogenation of (a) cyclohexane, (b) cyclohexene, and (c) cyclohexadiene. Free energy barriers (ΔG in kJ mol^{-1}) for each hydride acceptor species are reported at 623 K and referenced to their reactant state (ring adsorbed into proton- or alkyl-form zeolite). (d) Ratio of the rate of proton- to methyl-mediated dehydrogenation of cyclohexane (blue), cyclohexene (green), and cyclohexadiene (red) as a function of relative concentration of Z−H to Z−CH_3. Enthalpy (H), entropy (S), and free energy (G) values for transition states are reported in Figure 3. Additional values for reactant, product, and intermediate states are provided in Table S2 in the Supporting Information, with corresponding structures shown in Figure S16.

states (Figure 3). The transition states for proton-mediated hydride transfer reactions (Figure 3a−c) show a hydride far from the carbocation ring (1.6−1.8 Å) and closely coordinated with the proton from the zeolite (0.8−0.9 Å), a "late" transition state. Thus, it is likely that the cation is situated primarily on the ring and relatively far from the negatively charged surface. Conversely, methyl-mediated transition states (Figure 3d−f) were found to resemble a SN_2 transition state with a planar CH_3^+ carbocation between the hydride of cyclic species and the framework O atom. In this transition state, the cation is likely centered on CH_3^+, which is more closely coordinated with negatively charged zeolite (2.0−2.1 Å). These differences contribute to the lower activation energies for methyl-mediated pathways compared to proton-mediated paths.

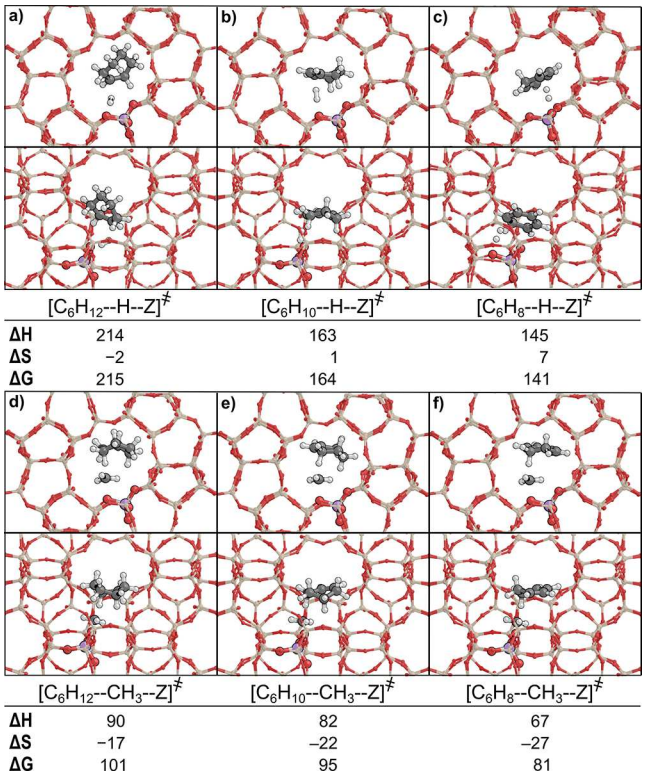

Figure 3. Lowest energy transition states for proton- (a−c) and methyl-mediated (d−f) dehydrogenation of cyclohexane, cyclohexene, and cyclohexadiene, respectively, with views down the straight (top) and sinusoidal (bottom) channels. Enthalpy (ΔH in kJ mol^{-1}), entropy (ΔS in J mol^{-1} K^{-1}), and free energy (ΔG in kJ mol^{-1}) barriers are reported at 623 K and relative to their corresponding most preceding state.

The rate of proton-mediated hydride transfer can be written as

$$r_{Z-H} = k_{HT,Z-H} K_{ads,Z-H} P_{C_6H_m} [Z - H] \quad (5)$$

where $k_{HT,Z-H}$ is the hydride transfer rate constant, $K_{ads,Z-H}$ is the equilibrium rate constant for ring adsorption near a proton, $P_{C_6H_m}$ is the gas-phase pressure of the ring species, and [Z−H] is the surface concentration of protons, respectively. Similarly, the rate of hydride transfer via the methyl-mediated pathway is

$$r_{Z-CH_3} = k_{HT,Z-CH_3} K_{ads,Z-CH_3} P_{C_6H_m} [Z - CH_3] \quad (6)$$

where $k_{HT,Z-CH_3}$ is the hydride transfer rate constant and $K_{ads,Z-CH3}$ is the equilibrium rate constant for ring adsorption near a surface methyl. Taking the ratio of Eq 5 to Eq 6 yields

$$\frac{r_{Z-H}}{r_{Z-CH_3}} = \frac{k_{HT,Z-H} K_{ads,Z-H}}{k_{HT,Z-CH_3} K_{ads,Z-CH_3}} \cdot \frac{[Z - H]}{[Z - CH_3]} = \exp\left(-\frac{\Delta\Delta G_{app}}{RT}\right) \frac{[Z - H]}{[Z - CH_3]} \quad (7)$$

where $\Delta\Delta G_{app}$ represents the difference in free energy barriers between methyl-mediated and proton-mediated dehydrogenation. This ratio is independent of the C_6H_m pressure, and the $(K_{ads,Z-H}/K_{ads,Z-CH_3})$ ratio accounts for any interactions between the adsorbed ring and Z−H or Z−CH_3. The kinetic relevance of proton-mediated and methyl-mediated dehydrogenation will be a function of the relative concentrations of Z−H and Z−CH_3 during MTO chemistries; eq 7 allows for direct comparison between methyl- and proton-mediated transition states as a function of the relative concentrations of Z−CH_3 and Z−H (Figure 2d). For equal concentrations of Z−CH_3

https://doi.org/10.1021/acscatal.2c03360
ACS Catal. 2023, 13, 99−112

and Z−H, the relative rates of proton-mediated pathways are >10^6 times smaller than those of methyl-mediated pathways. Given that surface-bound methyls are expected to be abundant surface intermediates during MTO, it is unlikely that dehydrogenation of ring compounds proceeds via proton-mediated hydride transfer, even at very early times on stream, and this prediction is consistent with that of most MTO studies not reporting H_2 as a product, while alkanes are observed including at low times on stream associated with the formation of aromatic compounds in the hydrocarbon pool.[2,18,99−106] The remainder of this work will emphasize alkyl-mediated hydride transfer pathways and examine the effects of ring saturation, ring substitution, and hydride acceptor substitution.

3.2. Contrasting Cycloalkane, Cycloalkene, and Cyclodiene Dehydrogenation Reactions. Cyclization of unsaturated species during MTO will form C_6 rings or methylated C_6 rings of varying saturations that subsequently dehydrogenate to form aromatic species (Scheme 3). For both

Scheme 3. Chemical Pathways for the Formation of Hydrocarbon Rings[a]

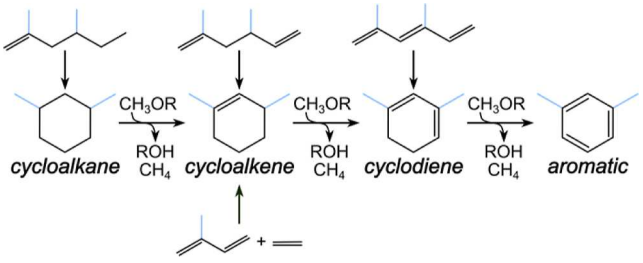

[a]Potential methyl substituents are shown in blue.

proton- and methyl-mediated routes, dehydrogenation barriers increase with the increasing degree of saturation (C_6H_{12} > C_6H_{10} > C_6H_8). The effects of saturation are more pronounced for the proton-mediated route, where Figure 2 shows trends in activation barriers of 215 > 164 > 151 kJ mol^{-1} for C_6H_{12}, C_6H_{10}, and C_6H_8, respectively. In proton-mediated routes, the positive charge of the transition state is located close to the ring, and more substituted rings can more effectively stabilize the cationic transition state, leading to lower barriers. The electronic gas-phase formation energies of these carbocations via hydride removal

$$C_6H_m \rightarrow C_6H_{m-1}^+ + H^-(g) \quad (8)$$

of $C_6H_{11}^+$, $C_6H_9^+$, and $C_6H_7^+$ are 1058, 994, and 931 kJ mol^{-1}, respectively. These energies trend with the corresponding activation barriers, suggesting that the greater ability of the dehydrogenated rings to accommodate positive charges leads to lower barriers. Conversely, in methyl-mediated routes, the cationic charge is mostly centered at the hydride-accepting species (CH_3^+), so the ability of the ring to stabilize positive charges becomes less relevant. This, in turn, results in less significant trends of activation barriers (101 > 95 > 81 kJ mol^{-1}) with ring desaturation.

A sequential reaction coordinate diagram for the conversion of cyclohexane into benzene is shown in Figure 4, for both MeOH (blue) and DME (red) as surface methylating agents. We chose cyclohexane and a surface methyl as a starting point, simply to show the broadest possible dehydrogenation sequence, and not as an endorsement of any cyclization

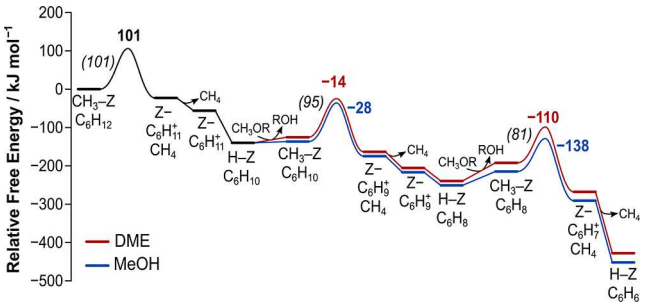

Figure 4. Reaction coordinate diagram for methyl-assisted dehydrogenation of cyclohexane to benzene with CH_3OH (blue) and CH_3OCH_3 (red) as surface methylating agents in MFI. Free energies (kJ mol^{-1}, 623 K) are reported referenced to physisorbed C_6H_{12} near a Z−CH_3. Enthalpy (H), entropy (S), and free energy (G) values are reported in Table S2 in the Supporting Information.

mechanism in MTO. Apparent free energy barriers, ΔG_{app}, of hydrogenation are 101, −14, and −110 kJ mol^{-1} for C_6H_{12}, C_6H_{10}, and C_6H_8, respectively, when DME acts as a surface methylating species (Figure 4). The large decreases in transition state formation energies suggest that at conditions relevant to MTO, the dehydrogenative aromatization of cyclohexane into benzene is exothermic and irreversible, irrespective of surface methylating species. The decrease in ΔG_{act} (Figure 4, italics) with increasing ring saturation suggests that the rate-limiting step of the dehydrogenation sequence will be the first hydride transfer, regardless of whether the sequence begins at a cycloalkane, cycloalkene, or cyclodiene. This conclusion that all hydride transfers are irreversible is also supported by maximum rate analysis examining the reversibility of each step over a broad range of potential reaction conditions (shown in Section S4 of the Supporting Information).

3.3. Dehydrogenation of C_7 and C_8 Hydrocarbon Rings: The Role of Methyl Substituents. Methylated cyclic compounds may also be formed from cyclization of C_7 or C_8 precursors that subsequently dehydrogenate to form methylbenzenes (Scheme 3). Here, we explore the dehydrogenation of methyl (C_7)- and dimethyl (C_8)- substituted rings to understand the role of methyl substituents on the dehydrogenation barriers of cycloalkanes, cycloalkenes, and cyclodienes.

We examined all double-bond isomers of C_7 and C_8 rings because the location of the methyl substituents and double bonds influences nearby hydride transfer reactions. For example, as shown in Figure 5, the C−H activation in methylcyclohexane may occur from a carbon atom at the geminal, ortho-, meta-, and para-positions relative to the methyl substituent. The corresponding activation free energies for these are 116−110 kJ mol^{-1} > 86−90 kJ mol^{-1}, respectively, suggesting that hydride transfers occur more favorably 2+ C atoms away from the methyl substituent. These findings trend opposite with gas-phase carbocation stabilities (Figure S5 in the Supporting Information), which suggest that carbocations are more stable when the cation is centered at the methylated carbon. Dehydrogenation barriers are governed by a combination of factors including carbocation stability and transition state interaction with the surrounding environment. These results suggest that additional methyl substituents do not offer enough additional carbocation stabilization (beyond ring conjugation) to overcome the steric hindrances between methyl substituents and hydride-accepting species (CH_3^+); as

https://doi.org/10.1021/acscatal.2c03360
ACS Catal. 2023, 13, 99−112

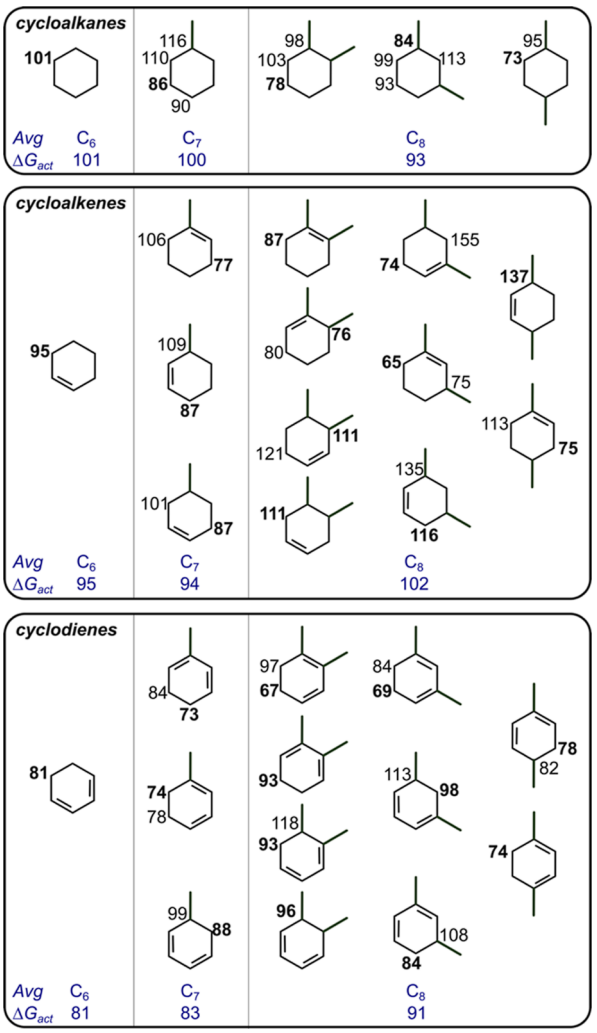

Figure 5. Free energy barriers for methyl-mediated dehydrogenation of cycloalkane, cycloalkene, and cyclodiene isomers in MFI. Barriers are shown next to the carbon atom participating in the C−H heterolytic cleavage that precedes the hydride transfer event. All unique locations were considered, except for cyclohexenes, where only those occurring immediately next to a double bond were considered. Enthalpy (H), entropy (S), and free energy (G) values for each transition state are reported in Table S3 of the Supporting Information, with corresponding structures shown in Figures S18−S21.

such, methyls proximal to dehydrogenation transition states increase barriers. Moreover, as discussed in Section 3.1, the transition state positive charge of methyl-mediated dehydrogenations is centered at the hydride-accepting species instead of the ring as in proton-mediated pathways; the carbocation placement of methyl-mediated dehydrogenation renders ring carbocation stabilities less relevant to transition state energies. Barriers are also lower for hydride transfers away from methyl substituents for reactions of all methylcyclohexene isomers and most methylcyclohexadiene isomers.

For the case of C_8 rings, we considered all skeletal and double-bond isomers. Hydride transfers generally occur with the lowest activation barriers away from the methyl substituents; there are exceptions, however, that suggest that steric hindrances govern barriers to a lesser extent. The convolution of effects caused by changes in sterics, carbocation stabilities, and the preferred shape of the transition states within these confining zeolite environments leads to weak correlations with the position of methyl substituents for C_8 species. Averaging the estimated barriers (shown in blue, Figure 5) shows that methyl substituents only slightly raise dehydrogenation barriers. These averaged values, however, do not account for potential double-bond isomerization events.

The interconversion between cycloalkene and cyclodiene double-bond isomers is governed by relative stability of each isomer, thus influencing the kinetically relevant pathways for hydrocarbon ring aromatization. Methylcyclohexane dehydrogenation occurs most favorably at the meta-position relative to the methyl substituent to form 4-methylcyclohexene (Figure 6). 4-Methylcyclohexene can either undergo a hydride transfer

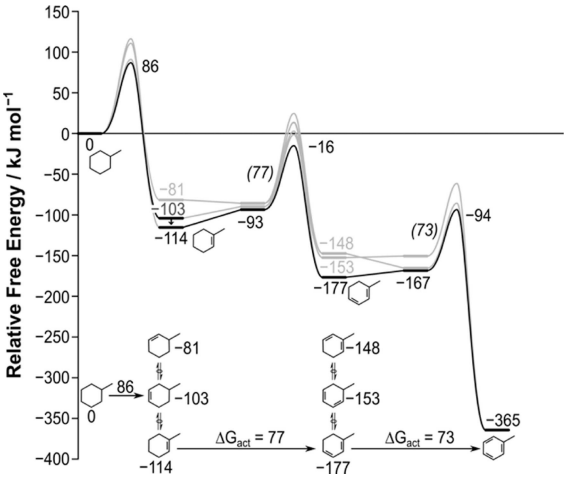

Figure 6. Reaction coordinate diagram for methyl-assisted dehydrogenation of methylcyclohexane to toluene with CH_3OH as the surface methylating agent in MFI. Free energies (kJ mol^{-1}, 623 K) are reported referenced to physiosorbed C_7H_{14} near Z−CH_3. The most favorable pathway is highlighted in black, with alternative pathways in gray. Reaction scheme shows both the conversion from C_7H_{14} into C_7H_8 and the isomerization between C_7H_{12} and C_7H_{10} double-bond isomers. Enthalpy (H), entropy (S), and free energy (G) values for reactant, product, and transition states are reported in Table S4 in the Supporting Information, with corresponding structures shown in Figures S17 and S18.

at the meta to the methyl substituent and ortho to the double bond (Figure 5) with a barrier of 87 kJ mol^{-1} or isomerize to form more stable 1-methylcyclohexene and subsequently dehydrogenate at the position meta to the methyl with a lower barrier (77 kJ mol^{-1}). The dehydrogenation of 1-methylcyclohexene forms 1-methyl-1,3-cyclohexadiene, the most stable methylcyclohexadiene isomer, which dehydrogenates to toluene with a ΔG_{act} of 73 kJ mol^{-1}. The overall route (Figure 6), involving hydride transfer, deprotonation, and double-bond isomerization, forms toluene with lower hydride transfer barriers (86, 77, and 73 kJ mol^{-1}) than that observed for the dehydrogenation of cyclohexane to benzene (101, 95, and 81 kJ mol^{-1}), despite steric hindrances. Ultimately, while methyl substituents discourage hydride transfer reactions at geminal and ortho positions relative to the substituent, this does not slow aromatization because double-bond isomerization avoids the need to ever perform a hydride transfer reaction at either of those positions. Indeed, the hydride transfer reactions of these C_7 species occur at positions meta, meta, and para to the methyl substituent. These conclusions are consistent for the aromatization of C_8 cycloalkanes

https://doi.org/10.1021/acscatal.2c03360
ACS Catal. 2023, 13, 99−112

(Figures S7−S9 in the Supporting Information), where double-bond isomerization allows dehydrogenation steps to occur away from the methyl substituents.

3.4. Alkyl-Mediated Pathways: The Role of Degree of Substitution from Hydride Transfer Acceptors on Dehydrogenation Barriers. Olefins, formed as products during MTO, can covalently bind to the framework as surface-bound alkyl species (Z−CR_3) and participate in further reactions. Previous work in MFI investigating C_1−C_4 alkyls as hydride acceptors in hydride transfer reactions with methanol and 2-butene found that increasing alkyl substitution stabilized the carbocation transition state, but this benefit is mitigated by steric penalties as the alkyl chain length increases.[39] Methanol preferentially reacts with tertiary *tert*-butyl, and 2-butene prefers to react with secondary 2-propyl even at respective Z−CR_3 concentrations 10^{-10} times lower than that of Z−CH_3, suggesting that olefin products facilitate hydride transfer of methanol (to form formaldehyde) and 2-butene (to form butadiene). Here, we will investigate the effect of carbocation substitution of the hydride acceptor on dehydrogenation rates with cyclohexane, cyclohexene, and cyclohexadiene.

Alkenes can adsorb into zeolite environments to form H-bonded alkenes that interact with Brønsted acid sites through π-bonding, can protonate to form charged alkenium species, or form a covalent C−O bond and exist as a surface-bound alkyl (see Figure S22 in the Supporting Information). The relative stability between these three binding modes—surface-bound alkyls, alkeniums, and H-bonded alkenes—was studied for small alkenes in H-FER using hybrid DFT and molecular MP2 calculations (PBE + D2 and ΔCCSD(T))[107] and in MFI using ab initio molecular dynamics.[108] These studies predict different binding modes as the most thermodynamically favorable; however, experimental studies in MFI indicate that double-bond isomerization is facile relative to C−C bond formation (473−856 K),[94,109−111] suggesting that interconversion between the three binding modes should occur readily. The dehydrogenation of hydrocarbon rings may also be mediated by these product-derived species. The role of carbocation substitution on dehydrogenation barriers was investigated by exploring ethene, propene, and isobutene species as these yield primary (C_2), secondary (C_3), and tertiary (C_4) carbocations.

Adsorption free energies (ΔG_{ads}, 623 K, 1 bar) shown in Figure 7 suggest that ethene binds as a H-bonded species with an adsorption energy (27 kJ mol^{-1}) that is ∼10 kJ mol^{-1} higher (less stable) than as a surface-bound ethyl species (ΔG_{ads} of 17 kJ mol^{-1}). For propene, in contrast, the H-bound species is (ΔG_{ads} of 24 kJ mol^{-1}) approximately 5 kJ mol^{-1} more stable than the secondary alkyl (30 kJ mol^{-1}), which is more stable than the primary alkyl (36 kJ mol^{-1}). For isobutene, our calculations suggest that H-bonded alkene is the most stable form, similar to propene, with the next most stable being the primary alkyl, followed by the sterically hindered tertiary alkyl, and finally the free carbocation. Across all three species, our ΔG_{ads} values suggest that bound species are less stable compared to values reported in MFI (for C_4)[108] and TON (C_2−C_4).[111] Some differences may arise from different confining voids (TON vs MFI) or different T-sites within MFI (T11 in our work and T12 in the prior work examining isobutene in MFI). This work, however, reports values as the most stable alkyl or H-bound alkene referenced to the most stable proton structures, regardless of the O atoms involved in either species. The most stable proton at T11 in our work is at

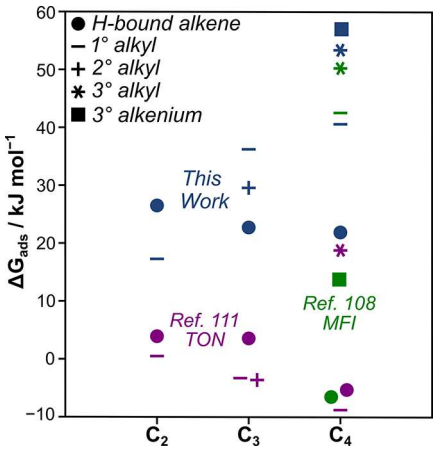

Figure 7. ΔG_{ads} (kJ mol^{-1}, 623 K) relative to a bare site and the corresponding gas-phase alkene (ethene, propene, or isobutene) for C_2, C_3, and C_4 surface-bound alkyls (−, +, and * respectively), H-bonded alkenes (circles), and alkeniums (squares). Values from this work are shown in blue along values from prior works on MFI[108] and TON[111] shown in green and purple, respectively. Enthalpy (H), entropy (S), and free energy (G) values for each binding mode are reported in Table S5 in the Supporting Information, with corresponding structures shown in Figure S22.

O16 and forms an H-bond to nearby framework O-atoms that must be broken to form a H-bound alkene, alkyl, or carbocation. This intraframework H-bond contributes to the higher ΔG_{ads} and is not observed without a rigorous sampling of the potential energy surface (see Section 2).

Regardless of the binding mode of these olefins, they can act as hydride-accepting species during ring dehydrogenation. The transition state structures for alkyl-mediated cyclohexane dehydrogenation are shown in Figure 8, with analogous figures for cyclohexene and cyclohexadiene dehydrogenation shown in Figure S23 in the Supporting Information. These transition state structures show that larger alkyls (more stable as carbocations) are more loosely coordinated to the conjugate base of the zeolite, thus resulting in larger C−O distances between the center (sp^2 C) of the carbocation and the nearest O atom of the conjugate base (AlO_4^-).

The ΔG_{act} values for alkyl-mediated routes, referenced to the hydrocarbon ring adsorbed near the corresponding Z−CR_3 state, decrease as the alkyl becomes more substituted (circles in Figure 9), consistent with more substituted alkyls forming more stable carbocations. These intrinsic barriers, however, do not account for the preference of propene and isobutene to exist as H-bound alkenes rather than adsorbed alkyls. Reporting ΔG_{act} values relative to these H-bound alkenes increases barriers for those reactions by 15−80 kJ mol^{-1} (squares in Figure 9). Furthermore, these ΔG_{act} values do not account for steric penalties associated with the colocation of the ring and the alkene (C_3 and C_4) or alkyl (C_1 and C_2) species. These steric effects are included by reporting a barrier referenced to the most stable alkyl or H-bonded alkene and a desorbed ring species (here called an apparent free energy barrier; diamonds in Figure 9). These apparent barriers show that the steric effects are generally larger for more substituted species, with the most dramatic repulsions felt near cyclohexane. Comparing apparent barriers, which are most relevant to the relative rates of these reactions, cyclohexane prefers to react with methyl and ethyl species, cyclohexene with propene, and cyclohexadiene with *t*-butyl. These trends may be

https://doi.org/10.1021/acscatal.2c03360
ACS Catal. 2023, 13, 99−112

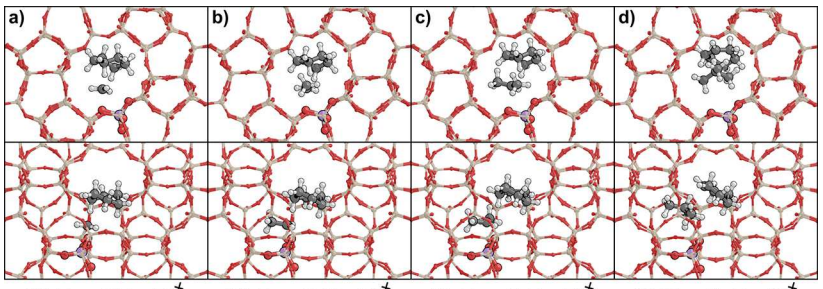

Figure 8. Lowest energy transition states: (a) methyl-, (b) ethyl-, (c) 2-propyl-, and (d) *tert*-butyl-mediated dehydrogenation of cyclohexane with views down the straight (top) and sinusoidal (bottom) channels. Enthalpy (ΔH in kJ mol^{-1}), entropy (ΔS in J mol^{-1} K^{-1}), and free energy (ΔG in kJ mol^{-1}) barriers are reported at 623 K and relative to the gas-phase ring and the corresponding best binding mode for alkene. Barriers relative to the ring near the surface-bound alkyl are reported in italics. Enthalpy (H), entropy (S), and free energy (G) values for cyclohexene and cyclohexadiene transition states are reported in Table S6 in the Supporting Information, with corresponding structures shown in Figure S23.

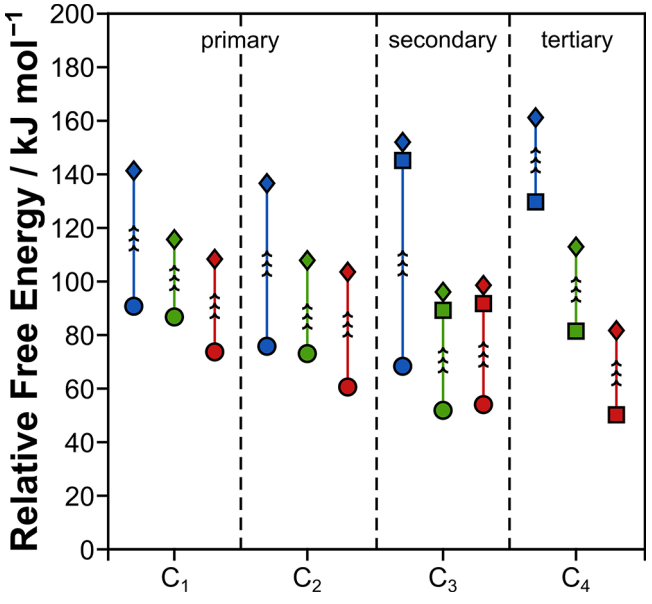

Figure 9. Free energy barriers for cyclohexane (blue), cyclohexene (green), and cyclohexadiene (red) dehydrogenations as a function of degree of substitution of hydride-accepting species. Free energies are reported at 623 K and relative to the ring near the adsorbed alkyl (circles), ring near the best alkene-binding mode (squares), and gas-phase ring + best binding mode (diamonds). Enthalpy (H), entropy (S), and free energy (G) values for each transition state are reported in Table S6 in the Supporting Information with corresponding structures shown in Figure S23.

rationalized from a competition between carbocation stability of hydride-accepting species and the sterics associated with the size from both the hydride acceptor and hydrocarbon ring species.

For example, cyclohexadiene dehydrogenation occurs preferentially with *tert*-butyl (ΔG_{act} = 82 kJ mol^{-1}), the most stable carbocation among the explored hydride acceptors. For cyclohexene, however, steric hindrances outweigh the favorability of the *tert*-butenium cation, rendering a slight preference for reaction with propene. For cyclohexane, carbocation stabilities are nullified even further, resulting in a preference for reaction with methyl and ethyl. Overall, reactant- and product-derived species act as hydride acceptors during the dehydrogenation of hydrocarbon rings, and their preferences are dictated by the hydrocarbon ring size, which in turn influences the competition between sterics and carbocation stabilities.

The implications of trends in activation barriers can be kinetically explored by the rate ratio between C_n-alkyl-mediated pathways to those mediated by methyls, given by

$$\frac{r_{Z-C_n}}{r_{Z-CH_3}} = \frac{k_{HT,Z-CN}K_{ads,Z-CN}}{k_{HT,Z-CH_3}K_{ads,Z-CH_3}} \cdot \frac{[C_n]}{[Z-CH_3]} = \exp\left(-\frac{\Delta\Delta G_{app}}{RT}\right)\frac{[C_n]}{[Z-CH_3]} \quad (9)$$

where $k_{HT,Z-CN}$ is the rate constant for the hydride transfer reaction to a C_N carbocation (barriers shown in Figure 9), $K_{ads,Z-CN}$ is the adsorption equilibrium constant for the ring reactant to a site adjacent to the C_N species, and $[C_N]$ is the concentration of the C_N species (present as either a H-bonded alkene, carbocation, or covalently bound alkyl species). Thus, as with the rate ratio shown in Figure 2d, this rate ratio will include coadsorbate interactions between ring reactants and the C_N species.

Figure 10 shows the ratio of rates for alkyl-mediated routes to their methyl-mediated counterpart, as a function of their relative surface coverages; methyl-mediated routes are favored at values below unity, while alkyl-mediated routes are favored at values above unity. At equal concentrations of all surface-bound species ($Z-C_n/Z-CH_3$ = 1), cyclohexane dehydrogenation occurs with ethyl as the hydride acceptor, and the relative rates of cyclohexane dehydrogenation decrease as the degree of substitution on the hydride acceptor increases. *tert*-Butyl-mediated dehydrogenations dominate over methyl-mediated ones only at high relative coverages of *tert*-butyl to methyl (>100×) despite barriers of *tert*-butyl-mediated hydride transfer, when referenced to an alkyl with co-adsorbed cyclohexane, being lower than methyl-mediated routes. Hydride transfer reactions benefit from increasing hydride acceptor substitution as well as suffer from steric hindrances of bulkier transition states. The aforementioned reference state does not capture sterics associated with forming bulkier transition states and, as such, incorrectly predicts the most favorable hydride acceptor. Instead, the ΔG_{app} value of Eq 9, referenced to an adsorbed alkyl and gas-phase ring,

https://doi.org/10.1021/acscatal.2c03360
ACS Catal. 2023, 13, 99−112

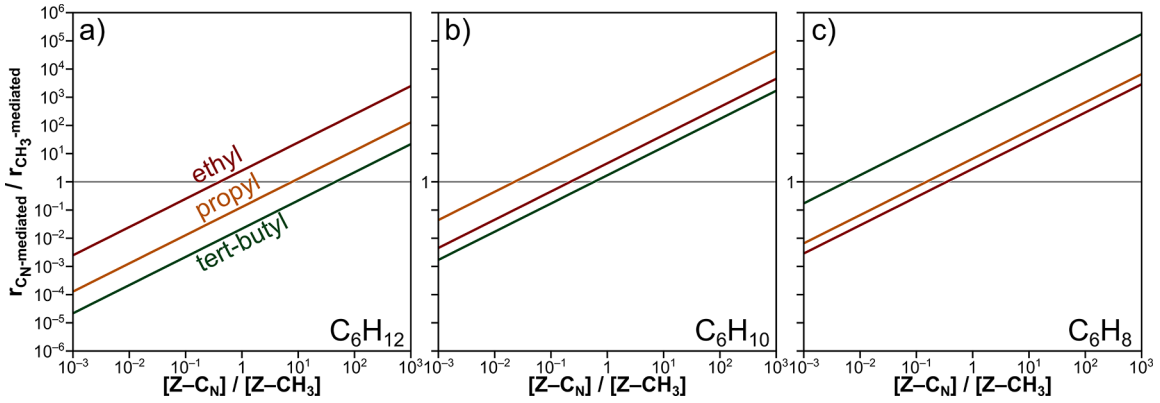

Figure 10. Ratio of the rate of ethyl- (red), 2-propyl- (orange), and *tert*-butyl (green)-mediated to methyl-mediated dehydrogenation of (a) cyclohexane, (b) cyclohexene, and (c) cyclohexadiene as a function of ratio of surface-bound species ($Z\text{–}C_N$) to methyls ($Z\text{–}CH_3$). Rates are reported at 623 K.

incorporates both benefits from increasing hydride acceptor substitution and steric hindrances of adsorbing a ring and is a more appropriate reference state to use in these reactions. In the case of cyclohexane, the steric hindrances associated with bulky transition states outweigh any benefits conferred by a more stable hydride acceptor—making methyls and ethyls the most favorable acceptors. Cyclohexadiene, however, is smaller than cyclohexane, which alleviates some of the sterics during reaction of C_3 and C_4 hydride acceptors and shows rate ratios above unity for both propyl and *t*-butyl even at relatively low concentrations to that of methyl (10^{-1} and 10^{-2}, respectively).

4. CONCLUSIONS

The dehydrogenation of saturated C_6 hydrocarbon rings via proton-mediated and alkyl-mediated routes was investigated in MFI framework zeolites. Dehydrogenation reactions occur by sequential hydride transfer followed by deprotonation reactions. Reactions were examined using protons as hydride acceptors as well as surface-bound alkyls (e.g., methyl groups). Activation barriers from proton-mediated routes trend with the degree of ring saturation, which can be rationalized by the relative stabilities of the transition-state carbocations ($C_6H_7^+$ > $C_6H_9^+$ > $C_6H_{11}^+$). The same trends are also observed for methyl-mediated routes, however, to a lesser extent because the positive charge of the transition state is at the hydride-accepting species (CH_3^+) rather than at the ring. Hydride transfers via methyl-mediated routes occur with free energy barriers >60 kJ mol^{-1}, which is lower than proton-mediated routes. These large differences in free energy barriers suggest that, once a hydrocarbon pool is present, proton-mediated hydride transfer reactions do not occur at relevant rates.

Free energy barriers for dehydrogenation of C_6 rings with a single methyl substituent are sensitive to the location of the methyl substituent relative to the hydride transfer event. When methyl substituents are at the geminal and ortho-positions, hydride transfer activation barriers are 32 and 26 kJ mol^{-1}, that is, larger compared to the non-methylated counterpart. Methyl substituents at the meta- and para-positions have little impact on hydride transfer barriers. The larger barriers associated with steric hindrances at geminal and ortho-positions, however, do not delay rates of C_7 dehydrogenation. Instead, rapid double-bond isomerization occurs, which allows the reactions from methylcyclohexane to toluene to proceed without sterically hindered hydride transfer events that govern the predominant pathways that yield methylbenzenes. The addition of a second methyl substituent (i.e., in hydride transfer reactions of C_8 species) yields no clear correlation between the location of methyl substituents with estimated activation barriers. This is likely due to other competing aspects during ring dehydrogenation events, such as the relative carbocation stabilities and more pronounced confinement effects from the zeolite framework that are inherent in bulkier molecules.

MTO mainly produces ethylene and propylene; however, larger alkenes can also be formed from subsequent methylation reactions, and all these larger hydrocarbons can serve as hydride acceptors. As such, we also examined ethyl-, propyl-, and *t*-butyl-assisted dehydrogenations of cyclic compounds. Dehydrogenation free energy barriers, relative to an adsorbed ring and alkyl, generally decrease as the hydride acceptor becomes more substituted and, thus, a more stable carbocation. However, steric effects between the ring and hydride acceptor do penalize the relative rates of hydride transfer reactions involving larger hydride acceptors. Rate ratios suggest that the preferred alkyl hydride acceptor depends on the size of the ring compound: C_6H_{12} dehydrogenation preferentially occurs with methyl and ethyl hydride acceptors, while C_6H_8 reacts with propyl and *tert*-butyl. The dehydrogenation of cyclization products during MTO occurs favorably via both reactant- and product-derived species (surface-bound methyls and larger alkyls, respectively), with relative rates governed by the unsteady-state evolution of the abundant surface intermediates and the relative concentrations of potential hydride-accepting species.

The conclusions presented here provide the fundamental rationale of the governing parameters that mediate ring dehydrogenation over H-MFI zeolites: a competition between the (1) inherent carbocation stability from hydride accepting species and (2) steric hindrances that occur between the hydrocarbon ring and hydride-accepting species. The extent to which these two parameters compete is likely governed by zeolite topology; smaller voids will exacerbate steric hindrances, while larger voids will likely favor more stable carbocations. These dehydrogenation reactions will be combined with subsequent studies on cyclization reactions to elucidate the kinetically relevant steps that mediate the interconversion between olefin- and aromatic-based cycles in MTO.

https://doi.org/10.1021/acscatal.2c03360
ACS Catal. 2023, 13, 99−112

■ ASSOCIATED CONTENT

Supporting Information

The Supporting Information is available free of charge at https://pubs.acs.org/doi/10.1021/acscatal.2c03360.

Details on temperature-corrected DFT enthalpies, entropies, and free energies; structural model for H-MFI and T11; reaction coordinate diagram for the proton-mediated dehydrogenation of cyclohexane into benzene; maximum rate analysis for proton- and methyl-mediated dehydrogenation of cyclohexane, cyclohexene, and cyclohexadiene; gas-phase C_6−C_8 carbocation formation energies; reaction coordinate diagrams for methyl-mediated dehydrogenation of C_8 cyclohexanes into xylenes; and reactant, product, and transition state structures with their corresponding enthalpies, entropies, and free energies (PDF)

■ AUTHOR INFORMATION

Corresponding Author

David Hibbitts − *Department of Chemical Engineering, University of Florida, Gainesville, Florida 32611, United States;* orcid.org/0000-0001-8606-7000; Email: hibbitts@che.ufl.edu

Authors

Hansel Montalvo-Castro − *Department of Chemical Engineering, University of Florida, Gainesville, Florida 32611, United States;* orcid.org/0000-0001-8833-7668

Mykela DeLuca − *Department of Chemical Engineering, University of Florida, Gainesville, Florida 32611, United States*

Lauren Kilburn − *Department of Chemical Engineering, University of Florida, Gainesville, Florida 32611, United States*

Complete contact information is available at: https://pubs.acs.org/10.1021/acscatal.2c03360

Notes

The authors declare no competing financial interest.

■ ACKNOWLEDGMENTS

This work was funded by an NSF CAREER award (1942684-CBET). Computational resources were provided by the Extreme Science and Engineering Discovery Environment (XSEDE), which is supported by the National Science Foundation grant no ACI-1548562.

■ REFERENCES

(1) Wang, C.-M.; Wang, Y.-D.; Liu, H.-X.; Yang, G.; Du, Y.-J.; Xie, Z.-K. Aromatic-Based Hydrocarbon Pool Mechanism for Methanol-to-Olefins Conversion in H-SAPO-18: A van Der Waals Density Functional Study. *Chin. J. Catal.* **2015**, *36*, 1573−1579.

(2) Hwang, A.; Prieto-Centurion, D.; Bhan, A. Isotopic Tracer Studies of Methanol-to-Olefins Conversion over HSAPO-34: The Role of the Olefins-Based Catalytic Cycle. *J. Catal.* **2016**, *337*, 52−56.

(3) Dejaifve, P.; Védrine, J. C.; Bolis, V.; Derouane, E. Reaction Pathways for the Conversion of Methanol and Olefins on H-ZSM-5 Zeolite. *J. Catal.* **1980**, *63*, 331−345.

(4) Wang, S.; Chen, Y.-Y.; Wei, Z.; Qin, Z.; Ma, H.; Dong, M.; Li, J.; Fan, W.; Wang, J. Polymethylbenzene or Alkene Cycle? Theoretical Study on Their Contribution to the Process of Methanol to Olefins over H-ZSM-5 Zeolite. *J. Phys. Chem. C* **2015**, *119*, 28482−28498.

(5) Sun, X.; Mueller, S.; Shi, H.; Haller, G. L.; Sanchez-Sanchez, M.; van Veen, A. C.; A. C; Lercher, J. A. On the Impact of Co-Feeding Aromatics and Olefins for the Methanol-to-Olefins Reaction on HZSM-5. *J. Catal.* **2014**, *314*, 21−31.

(6) Wang, C.-M.; Wang, Y.-D.; Xie, Z.-K. Verification of the Dual Cycle Mechanism for Methanol-to-Olefin Conversion in HSAPO-34: A Methylbenzene-Based Cycle from DFT Calculations. *Catal. Sci. Technol.* **2014**, *4*, 2631−2638.

(7) Arstad, B.; Nicholas, J. B.; Haw, J. F. Theoretical Study of the Methylbenzene Side-Chain Hydrocarbon Pool Mechanism in Methanol to Olefin Catalysis. *J. Am. Chem. Soc.* **2004**, *126*, 2991−3001.

(8) Janssens, T. V. W.; Svelle, S.; Olsbye, U. Kinetic Modeling of Deactivation Profiles in the Methanol-to-Hydrocarbons (MTH) Reaction: A Combined Autocatalytic−hydrocarbon Pool Approach. *J. Catal.* **2013**, *308*, 122−130.

(9) Wang, C.; Chu, Y.; Zheng, A.; Xu, J.; Wang, Q.; Gao, P.; Qi, G.; Gong, Y.; Deng, F. New Insight into the Hydrocarbon-Pool Chemistry of the Methanol-to-Olefins Conversion over Zeolite H-ZSM-5 from GC-MS, Solid-State NMR Spectroscopy, and DFT Calculations. *Chem.—Eur. J* **2014**, *20*, 12432−12443.

(10) Hemelsoet, K.; Van der Mynsbrugge, J.; De Wispelaere, K.; Waroquier, M.; Van Speybroeck, V. Unraveling the Reaction Mechanisms Governing Methanol-to-Olefins Catalysis by Theory and Experiment. *ChemPhysChem* **2013**, *14*, 1526−1545.

(11) Bollini, P.; Bhan, A. Improving HSAPO-34 Methanol-to-Olefin Turnover Capacity by Seeding the Hydrocarbon Pool. *ChemPhysChem* **2018**, *19*, 479−483.

(12) Seiler, M.; Wang, W.; Buchholz, A.; Hunger, M. Direct Evidence for a Catalytically Active Role of the Hydrocarbon Pool Formed on Zeolite H-ZSM-5 during the Methanol-to-Olefin Conversion. *Catal. Lett.* **2003**, *88*, 187−191.

(13) Wang, S.; Chen, Y.; Qin, Z.; Zhao, T.-S.; Fan, S.; Dong, M.; Li, J.; Fan, W.; Wang, J. Origin and Evolution of the Initial Hydrocarbon Pool Intermediates in the Transition Period for the Conversion of Methanol to Olefins over H-ZSM-5 Zeolite. *J. Catal.* **2019**, *369*, 382−395.

(14) Wang, C.; Xu, J.; Qi, G.; Gong, Y.; Wang, W.; Gao, P.; Wang, Q.; Feng, N.; Liu, X.; Deng, F. Methylbenzene Hydrocarbon Pool in Methanol-to-Olefins Conversion over Zeolite H-ZSM-5. *J. Catal.* **2015**, *332*, 127−137.

(15) Hill, I. M.; Hashimi, S. A.; Bhan, A. Kinetics and Mechanism of Olefin Methylation Reactions on Zeolites. *J. Catal.* **2012**, *285*, 115−123.

(16) Ilias, S.; Bhan, A. Mechanism of the Catalytic Conversion of Methanol to Hydrocarbons. *ACS Catal.* **2013**, *3*, 18−31.

(17) Wang, S.; Agirrezabal-Telleria, I.; Bhan, A.; Simonetti, D.; Takanabe, K.; Iglesia, E. Catalytic Routes to Fuels from C1 and Oxygenate Molecules. *Faraday Discuss.* **2017**, *197*, 9−39.

(18) Hwang, A.; Kumar, M.; Rimer, J. D.; Bhan, A. Implications of Methanol Disproportionation on Catalyst Lifetime for Methanol-to-Olefins Conversion by HSSZ-13. *J. Catal.* **2017**, *346*, 154−160.

(19) Lukyanov, D. B.; Gnep, N. S.; Guisnet, M. R. Kinetic Modeling of Ethene and Propene Aromatization over HZSM-5 and GaHZSM-5. *Ind. Eng. Chem. Res.* **1994**, *33*, 223−234.

(20) Joshi, Y. V.; Bhan, A.; Thomson, K. T. DFT-Based Reaction Pathway Analysis of Hexadiene Cyclization via Carbenium Ion Intermediates: Mechanistic Study of Light Alkane Aromatization Catalysis. *J. Phys. Chem. B* **2004**, *108*, 971−980.

(21) Joshi, Y.; Thomson, K. Embedded Cluster (QM/MM) Investigation of C6 Diene Cyclization in HZSM-5. *J. Catal.* **2005**, *230*, 440−463.

(22) Joshi, Y. V.; Thomson, K. T. Brønsted Acid Catalyzed Cyclization of C7 and C8 Dienes in HZSM-5: A Hybrid QM/MM Study and Comparison with C6 Diene Cyclization. *J. Phys. Chem. C* **2008**, *112*, 12825−12833.

(23) Wang, C.-M.; Wang, Y.-D.; Xie, Z.-K.; Liu, Z.-P. Methanol to Olefin Conversion on HSAPO-34 Zeolite from Periodic Density Functional Theory Calculations: A Complete Cycle of Side Chain

Hydrocarbon Pool Mechanism. *J. Phys. Chem. C* **2009**, *113*, 4584−4591.
(24) Ilias, S.; Bhan, A. The Mechanism of Aromatic Dealkylation in Methanol-to-Hydrocarbons Conversion on H-ZSM-5: What Are the Aromatic Precursors to Light Olefins? *J. Catal.* **2014**, *311*, 6−16.
(25) Li, J.; Wei, Y.; Qi, Y.; Tian, P.; Li, B.; He, Y.; Chang, F.; Sun, X.; Liu, Z. Conversion of Methanol over H-ZSM-22: The Reaction Mechanism and Deactivation. *Catal. Today* **2011**, *164*, 288−292.
(26) Martinez-Espin, J. S.; Mortén, M.; Janssens, T. V. W.; Svelle, S.; Beato, P.; Olsbye, U. New Insights into Catalyst Deactivation and Product Distribution of Zeolites in the Methanol-to-Hydrocarbons (MTH) Reaction with Methanol and Dimethyl Ether Feeds. *Catal. Sci. Technol.* **2017**, *7*, 2700−2716.
(27) Dai, W.; Wu, G.; Li, L.; Guan, N.; Hunger, M. Mechanisms of the Deactivation of SAPO-34 Materials with Different Crystal Sizes Applied as MTO Catalysts. *ACS Catal.* **2013**, *3*, 588−596.
(28) Bjørgen, M.; Olsbye, U.; Kolboe, S. Coke Precursor Formation and Zeolite Deactivation: Mechanistic Insights from Hexamethylbenzene Conversion. *J. Catal.* **2003**, *215*, 30−44.
(29) Bjørgen, M.; Akyalcin, S.; Olsbye, U.; Benard, S.; Kolboe, S.; Svelle, S. Methanol to Hydrocarbons over Large Cavity Zeolites: Toward a Unified Description of Catalyst Deactivation and the Reaction Mechanism. *J. Catal.* **2010**, *275*, 170−180.
(30) Liu, Y.; Kirchberger, F. M.; Müller, S.; Eder, M.; Tonigold, M.; Sanchez-Sanchez, M.; Lercher, J. A. Critical Role of Formaldehyde during Methanol Conversion to Hydrocarbons. *Nat. Commun.* **2019**, *10*, 1462.
(31) Wang, S.; Iglesia, E. Mechanism of Isobutanal−isobutene Prins Condensation Reactions on Solid Brønsted Acids. *ACS Catal.* **2016**, *6*, 7664−7684.
(32) Dumitriu, E.; Trong On, D.; Kaliaguine, S. Isoprene by Prins Condensation over Acidic Molecular Sieves. *J. Catal.* **1997**, *170*, 150−160.
(33) Arundale, E.; Mikeska, L. A. The Olefin-Aldehyde Condensation. The Prins Reaction. *Chem. Rev.* **1952**, *51*, 505−555.
(34) Vasiliadou, E. S.; Gould, N. S.; Lobo, R. F. Zeolite-Catalyzed Formaldehyde-Propylene Prins Condensation. *ChemCatChem* **2017**, *9*, 4417−4425.
(35) Bedenko, S. P.; Kozhevnikov, A. A.; Dement'ev, K. I.; Tret'yakov, V. F.; Maximov, A. L. The Prins Condensation between I-Butene and Formaldehyde over Modified BEA and MFI Zeolites in Liquid Phase. *Catal. Commun.* **2020**, *138*, 105965.
(36) Kots, P. A.; Artsiusheuski, M. A.; Grigoriev, Y. V.; Ivanova, I. I. One-Step Butadiene Synthesis via Gas-Phase Prins Condensation of Propylene with Formaldehyde over Heteropolyacid Catalysts. *ACS Catal.* **2020**, *10*, 15149−15161.
(37) Yun, J. H.; Lobo, R. F. Effects of Temperature Pretreatment on Propane Cracking over H-SSZ-13 Zeolites. *Catal. Sci. Technol.* **2015**, *5*, 264−273.
(38) Sushkevich, V. L.; Ordomsky, V. V.; Ivanova, I. I. Synthesis of Isoprene from Formaldehyde and Isobutene over Phosphate Catalysts. *Appl. Catal., A* **2012**, *441*−*442*, 21−29.
(39) Kilburn, L.; DeLuca, M.; Hoffman, A. J.; Patel, S.; Hibbitts, D. Comparing Alkene-Mediated and Formaldehyde-Mediated Diene Formation Routes in Methanol-to-Olefins Catalysis in MFI and CHA. *J. Catal.* **2021**, *400*, 124−139.
(40) Fu, H.; Xie, S.; Fu, A.; Ye, T. Theoretical Study of the Carbonyl-Ene Reaction between Formaldehyde and Propylene on the MgY Zeolite. *Comput. Theor. Chem.* **2012**, *982*, 51−57.
(41) Wannakao, S.; Khongpracha, P.; Limtrakul, J. Density Functional Theory Study of the Carbonyl-Ene Reaction of Encapsulated Formaldehyde in Cu(I), Ag(I), and Au(I) Exchanged FAU Zeolites. *J. Phys. Chem. A* **2011**, *115*, 12486−12492.
(42) Sangthong, W.; Probst, M.; Limtrakul, J. Computational Study of the Carbonyl-Ene Reaction of Encapsulated Formaldehyde in Na-FAU Zeolite. *J. Mol. Struct.* **2005**, *748*, 119−127.
(43) Arora, S. S.; Bhan, A. The Critical Role of Methanol Pressure in Controlling Its Transfer Dehydrogenation and the Corresponding Effect on Propylene-to-Ethylene Ratio during Methanol-to-Hydrocarbons Catalysis on H-ZSM-5. *J. Catal.* **2017**, *356*, 300−306.
(44) Arora, S. S.; Nieskens, D. L. S.; Malek, A.; Bhan, A. Lifetime Improvement in Methanol-to-Olefins Catalysis over Chabazite Materials by High-Pressure H_2 Co-Feeds. *Nat. Catal.* **2018**, *1*, 666−672.
(45) Arora, S. S.; Shi, Z.; Bhan, A. Mechanistic Basis for Effects of High-Pressure H2 Cofeeds on Methanol-to-Hydrocarbons Catalysis over Zeolites. *ACS Catal.* **2019**, *9*, 6407−6414.
(46) Shi, Z.; Neurock, M.; Bhan, A. Methanol-to-Olefins Catalysis on HSSZ-13 and HSAPO-34 and Its Relationship to Acid Strength. *ACS Catal.* **2021**, *11*, 1222−1232.
(47) DeLuca, M.; Janes, C.; Hibbitts, D. Contrasting Arene, Alkene, Diene, and Formaldehyde Hydrogenation in H-ZSM-5, H-SSZ-13, and H-SAPO-34 Frameworks during MTO. *ACS Catal.* **2020**, *10*, 4593−4607.
(48) Hwang, A.; Bhan, A. Bifunctional Strategy Coupling Y_2 O_3 -Catalyzed Alkanal Decomposition with Methanol-to-Olefins Catalysis for Enhanced Lifetime. *ACS Catal.* **2017**, *7*, 4417−4422.
(49) Gao, D.; Zhi, Y.; Cao, L.; Zhao, L.; Gao, J.; Xu, C. Optimizing the Acid Properties of the HZSM-5 Catalyst for Increasing the p -Xylene Yield in 1-Hexene Aromatization. *Ind. Eng. Chem. Res.* **2022**, *61*, 3539−3549.
(50) Lee, J. S.; Caratzoulas, S.; Lobo, R. F. Carbocation-Mediated Cyclization of Trienes in Acid Zeolites. *J. Phys. Chem. A* **2021**, *125*, 4062−4069.
(51) Narayana Murthy, Y. V. S.; Pillai, C. N. Diels-Alder Reactions Catalyzed by Zeolites. *Synth. Commun.* **1991**, *21*, 783−791.
(52) Patet, R. E.; Nikbin, N.; Williams, C. L.; Green, S. K.; Chang, C.-C.; Fan, W.; Caratzoulas, S.; Dauenhauer, P. J.; Vlachos, D. G. Kinetic Regime Change in the Tandem Dehydrative Aromatization of Furan Diels−alder Products. *ACS Catal.* **2015**, *5*, 2367−2375.
(53) Green, S. K.; Patet, R. E.; Nikbin, N.; Williams, C. L.; Chang, C.-C.; Yu, J.; Gorte, R. J.; Caratzoulas, S.; Fan, W.; Vlachos, D. G.; Dauenhauer, P. J. Diels−Alder Cycloaddition of 2-Methylfuran and Ethylene for Renewable Toluene. *Appl. Catal., B* **2016**, *180*, 487−496.
(54) Williams, C. L.; Vinter, K. P.; Chang, C.-C.; Xiong, R.; Green, S. K.; Sandler, S. I.; Vlachos, D. G.; Fan, W.; Dauenhauer, P. J. Kinetic Regimes in the Tandem Reactions of H-BEA Catalyzed Formation of p-Xylene from Dimethylfuran. *Catal. Sci. Technol.* **2016**, *6*, 178−187.
(55) Shi, Z.; Arora, S. S.; Trahan, D. W.; Hickman, D.; Bhan, A. Methanol to Hydrocarbons Conversion: Why Dienes and Monoenes Contribute Differently to Catalyst Deactivation? *Chem. Eng. J.* **2022**, *437*, 134229.
(56) Foley, B. L.; Johnson, B. A.; Bhan, A. Kinetic Evaluation of Deactivation Pathways in Methanol-to-Hydrocarbon Catalysis on HZSM-5 with Formaldehyde, Olefinic, Dieneic, and Aromatic Co-Feeds. *ACS Catal.* **2021**, *11*, 3628−3637.
(57) Dass, D. Reactions of N-Alkanes over H-ZSM-5: Detection of Reactive Intermediates. *J. Catal.* **1988**, *113*, 259−262.
(58) Mériaudeau, P.; Naccache, C. Dehydrocyclization of Alkanes Over Zeolite-Supported Metal Catalysts: Monofunctional or Bifunctional Route. *Catal. Rev.* **1997**, *39*, 5−48.
(59) Wulfers, M. J.; Jentoft, F. C. The Role of Cyclopentadienium Ions in Methanol-to-Hydrocarbons Chemistry. *ACS Catal.* **2014**, *4*, 3521−3532.
(60) Giannetto, G.; Monque, R.; Galiasso, R. Transformation of LPG into Aromatic Hydrocarbons and Hydrogen over Zeolite Catalysts. *Catal. Rev.* **1994**, *36*, 271−304.
(61) Marques, J. P.; Gener, I.; Lopes, J. M.; Ribeiro, F. R.; Guisnet, M. Methylcyclohexane Transformation over Dealuminated HBEA Samples: Mechanisms and Active Sites. *Appl. Catal., A* **2006**, *301*, 96−105.
(62) Hungenberg, K. Evidence for a Diels-Alder Reaction between Dienes and Olefins in the Dehydrocyclodimerization of Butene-1 on Tellurium-Loaded Zeolites. *J. Catal.* **1981**, *68*, 200−202.
(63) Dogra, A.; Gupta, N. Aluminum-based Catalysts for Cycloaddition Reactions: Moving One Step Ahead in Sustainability. *ChemistrySelect* **2019**, *4*, 10452−10465.

https://doi.org/10.1021/acscatal.2c03360
ACS Catal. 2023, 13, 99−112

(64) Ishihara, A.; Kodama, Y.; Hashimoto, T. Aromatics Formation by Cracking and Dehydrocyclization of N-Hexane Using Zn Ion-Exchanged ZSM-5−Al2O3 Hierarchical Composite Catalysts. *React. Kinet., Mech. Catal.* **2021**, *134*, 401−417.
(65) Ishihara, A.; Mizuno, T.; Hashimoto, T. Effect of Type of Matrix on Formation of Aromatics by Cracking and Dehydrocyclization of n-Pentane Using ZnZSM-5 Metal Oxide Hierarchical Composite Catalysts. *J. Jpn. Petrol. Inst.* **2022**, *65*, 27−35.
(66) Guisnet, M.; Magnoux, P. Organic Chemistry of Coke Formation. *Appl. Catal., A* **2001**, *212*, 83−96.
(67) Chua, Y. T.; Stair, P. C. An Ultraviolet Raman Spectroscopic Study of Coke Formation in Methanol to Hydrocarbons Conversion over Zeolite H-MFI. *J. Catal.* **2003**, *213*, 39−46.
(68) Wang, C.; Hu, M.; Chu, Y.; Zhou, X.; Wang, Q.; Qi, G.; Li, S.; Xu, J.; Deng, F. π-Interactions between Cyclic Carbocations and Aromatics Cause Zeolite Deactivation in Methanol-to-Hydrocarbon Conversion. *Angew. Chem., Int. Ed.* **2020**, *59*, 7198−7202.
(69) Anderson, J. R.; Chang, Y. F.; Western, R. J. The Effect of Acidity on the Ormation of Retained Residue From-1-Hexene over Usy Zeolite Catalysts. *Catalyst Deactivation 1991, Proceedings of the 5th International Symposium; Studies in Surface Science and Catalysis*; Elsevier, 1991; Vol. *68*, pp 745−751.
(70) Anderson, J. Retained and Desorbed Products from Reaction of 1-Hexene over H-ZSM5 Zeolite: Routes to Coke Precursors. *J. Catal.* **1989**, *118*, 466−482.
(71) Choudhary, V. R.; Devadas, P.; Banerjee, S.; Kinage, A. K. Aromatization of Dilute Ethylene over Ga-Modified ZSM-5 Type Zeolite Catalysts. *Microporous Mesoporous Mater.* **2001**, *47*, 253−267.
(72) Kresse, G.; Hafner, J. Ab Initio Molecular Dynamics for Liquid Metals. *Phys. Rev. B: Condens. Matter Mater. Phys.* **1993**, *47*, 558−561.
(73) Kresse, G.; Hafner, J. Ab Initio Molecular-Dynamics Simulation of the Liquid-Metal-Amorphous-Semiconductor Transition in Germanium. *Phys. Rev. B: Condens. Matter Mater. Phys.* **1994**, *49*, 14251−14269.
(74) Kresse, G.; Furthmüller, J. Efficient Iterative Schemes for Ab Initio Total-Energy Calculations Using a Plane-Wave Basis Set. *Phys. Rev. B: Condens. Matter Mater. Phys.* **1996**, *54*, 11169−11186.
(75) Kresse, G.; Furthmüller, J. Efficiency of Ab-Initio Total Energy Calculations for Metals and Semiconductors Using a Plane-Wave Basis Set. *Comput. Mater. Sci.* **1996**, *6*, 15−50.
(76) Kravchenko, P.; Plaisance, C.; Hibbitts, D. A New Computational Interface for Catalysis. *ChemRxiv* **2019**, DOI: 10.26434/chemrxiv.8040737.v4. Published as pre-print on https://chemrxiv.org/articles/preprint/8040737
(77) Perdew, J. P.; Burke, K.; Ernzerhof, M. Generalized Gradient Approximation Made Simple. *Phys. Rev. Lett.* **1996**, *77*, 3865−3868.
(78) Zhang, Y.; Yang, W. Comment on "Generalized Gradient Approximation Made Simple". *Phys. Rev. Lett.* **1998**, *80*, 890.
(79) Hammer, B.; Hansen, L. B.; Nørskov, J. K. Improved Adsorption Energetics within Density-Functional Theory Using Revised Perdew-Burke-Ernzerhof Functionals. *Phys. Rev. B: Condens. Matter Mater. Phys.* **1999**, *59*, 7413−7421.
(80) Grimme, S.; Ehrlich, S.; Goerigk, L. Effect of the Damping Function in Dispersion Corrected Density Functional Theory. *J. Comput. Chem.* **2011**, *32*, 1456−1465.
(81) Schröder, H.; Creon, A.; Schwabe, T. Reformulation of the D3(Becke-Johnson) Dispersion Correction without Resorting to Higher than C_6 Dispersion Coefficients. *J. Chem. Theory Comput.* **2015**, *11*, 3163−3170.
(82) Grimme, S.; Antony, J.; Ehrlich, S.; Krieg, H. A Consistent and Accurate Ab Initio Parametrization of Density Functional Dispersion Correction (DFT-D) for the 94 Elements H-Pu. *J. Chem. Phys.* **2010**, *132*, 154104.
(83) van Koningsveld, H. High-Temperature (350 K) Orthorhombic Framework Structure of Zeolite H-ZSM-5. *Acta Crystallogr., Sect. B: Struct. Sci.* **1990**, *46*, 731−735.
(84) Hoffman, A.; DeLuca, M.; Hibbitts, D. Restructuring of MFI Framework Zeolite Models and Their Associated Artifacts in Density Functional Theory Calculations. *J. Phys. Chem. C* **2019**, *123*, 6572−6585.
(85) Database of zeolite structures. http://www.iza-structure.org/databases/ (accessed Jan 17, 2022).
(86) Ghorbanpour, A.; Rimer, J. D.; Grabow, L. C. Computational Assessment of the Dominant Factors Governing the Mechanism of Methanol Dehydration over H-ZSM-5 with Heterogeneous Aluminum Distribution. *ACS Catal.* **2016**, *6*, 2287−2298.
(87) Nimlos, C. T.; Hoffman, A. J.; Hur, Y. G.; Lee, B. J.; Di Iorio, J. R.; Hibbitts, D. D.; Gounder, R. Experimental and Theoretical Assessments of Aluminum Proximity in MFI Zeolites and Its Alteration by Organic and Inorganic Structure-Directing Agents. *Chem. Mater.* **2020**, *32*, 9277−9298.
(88) Monkhorst, H. J.; Pack, J. D. Special Points for Brillouin-Zone Integrations. *Phys. Rev. B: Solid State* **1976**, *13*, 5188−5192.
(89) Jónsson, H.; Mills, G.; Jacobsen, K. W. Nudged Elastic Band Method for Finding Minimum Energy Paths of Transitions. In *Classical and Quantum Dynamics in Condensed Phase Simulations*; Berne, B. J., Ciccotti, G., Coker, D. F., Eds.; World Scientific, 1998; pp 385−404.
(90) Henkelman, G.; Jónsson, H. A Dimer Method for Finding Saddle Points on High Dimensional Potential Surfaces Using Only First Derivatives. *J. Chem. Phys.* **1999**, *111*, 7010−7022.
(91) Martinez-Espin, J. S.; De Wispelaere, K.; Westgård Erichsen, M.; Svelle, S.; Janssens, T. V. W.; Van Speybroeck, V.; Beato, P.; Olsbye, U. Benzene Co-Reaction with Methanol and Dimethyl Ether over Zeolite and Zeotype Catalysts: Evidence of Parallel Reaction Paths to Toluene and Diphenylmethane. *J. Catal.* **2017**, *349*, 136−148.
(92) DeLuca, M.; Kravchenko, P.; Hoffman, A.; Hibbitts, D. Mechanism and Kinetics of Methylating C_6 −C_{12} Methylbenzenes with Methanol and Dimethyl Ether in H-MFI Zeolites. *ACS Catal.* **2019**, *9*, 6444−6460.
(93) Sarazen, M. L.; Doskocil, E.; Iglesia, E. Effects of Void Environment and Acid Strength on Alkene Oligomerization Selectivity. *ACS Catal.* **2016**, *6*, 7059−7070.
(94) Sarazen, M. L.; Doskocil, E.; Iglesia, E. Catalysis on Solid Acids: Mechanism and Catalyst Descriptors in Oligomerization Reactions of Light Alkenes. *J. Catal.* **2016**, *344*, 553−569.
(95) De Wispelaere, K.; Martínez-Espín, J. S.; Hoffmann, M. J.; Svelle, S.; Olsbye, U.; Bligaard, T. Understanding Zeolite-Catalyzed Benzene Methylation Reactions by Methanol and Dimethyl Ether at Operating Conditions from First Principle Microkinetic Modeling and Experiments. *Catal. Today* **2018**, *312*, 35−43.
(96) De Wispelaere, K.; Bailleul, S.; Van Speybroeck, V. Towards Molecular Control of Elementary Reactions in Zeolite Catalysis by Advanced Molecular Simulations Mimicking Operating Conditions. *Catal. Sci. Technol.* **2016**, *6*, 2686−2705.
(97) Brogaard, R. Y.; Henry, R.; Schuurman, Y.; Medford, A. J.; Moses, P. G.; Beato, P.; Svelle, S.; Nørskov, J. K.; Olsbye, U. Methanol-to-Hydrocarbons Conversion: The Alkene Methylation Pathway. *J. Catal.* **2014**, *314*, 159−169.
(98) Jones, A. J.; Iglesia, E. Kinetic, Spectroscopic, and Theoretical Assessment of Associative and Dissociative Methanol Dehydration Routes in Zeolites. *Angew. Chem., Int. Ed.* **2014**, *53*, 12177−12181.
(99) Khare, R.; Liu, Z.; Han, Y.; Bhan, A. A Mechanistic Basis for the Effect of Aluminum Content on Ethene Selectivity in Methanol-to-Hydrocarbons Conversion on HZSM-5. *J. Catal.* **2017**, *348*, 300−305.
(100) Svelle, S.; Joensen, F.; Nerlov, J.; Olsbye, U.; Lillerud, K.-P.; Kolboe, S.; Bjørgen, M. Conversion of Methanol into Hydrocarbons over Zeolite H-ZSM-5: Ethene Formation Is Mechanistically Separated from the Formation of Higher Alkenes. *J. Am. Chem. Soc.* **2006**, *128*, 14770−14771.
(101) Khare, R.; Bhan, A. Mechanistic Studies of Methanol-to-Hydrocarbons Conversion on Diffusion-Free MFI Samples. *J. Catal.* **2015**, *329*, 218−228.
(102) Sun, X.; Mueller, S.; Liu, Y.; Shi, H.; Haller, G. L.; Sanchez-Sanchez, M.; van Veen, A. C.; Lercher, J. A. On Reaction Pathways in

the Conversion of Methanol to Hydrocarbons on HZSM-5. *J. Catal.* **2014**, *317*, 185−197.
(103) Müller, S.; Liu, Y.; Vishnuvarthan, M.; Sun, X.; van Veen, A. C.; Haller, G. L.; Sanchez-Sanchez, M.; Lercher, J. A. Coke Formation and Deactivation Pathways on H-ZSM-5 in the Conversion of Methanol to Olefins. *J. Catal.* **2015**, *325*, 48−59.
(104) Müller, S.; Liu, Y.; Kirchberger, F. M.; Tonigold, M.; Sanchez-Sanchez, M.; Lercher, J. A. Hydrogen Transfer Pathways during Zeolite Catalyzed Methanol Conversion to Hydrocarbons. *J. Am. Chem. Soc.* **2016**, *138*, 15994−16003.
(105) Hereijgers, B. P. C.; Bleken, F.; Nilsen, M. H.; Svelle, S.; Lillerud, K.-P.; Bjørgen, M.; Weckhuysen, B. M.; Olsbye, U. Product Shape Selectivity Dominates the Methanol-to-Olefins (MTO) Reaction over H-SAPO-34 Catalysts. *J. Catal.* **2009**, *264*, 77−87.
(106) Bleken, F. L.; Chavan, S.; Olsbye, U.; Boltz, M.; Ocampo, F.; Louis, B. Conversion of Methanol into Light Olefins over ZSM-5 Zeolite: Strategy to Enhance Propene Selectivity. *Appl. Catal., A* **2012**, *447*−*448*, 178−185.
(107) Ren, Q.; Rybicki, M.; Sauer, J. Interaction of C_3 −C_5 Alkenes with Zeolitic Brønsted Sites: π-Complexes, Alkoxides, and Carbenium Ions in H-FER. *J. Phys. Chem. C* **2020**, *124*, 10067−10078.
(108) Cnudde, P.; De Wispelaere, K.; Van der Mynsbrugge, J.; Waroquier, M.; Van Speybroeck, V. Effect of Temperature and Branching on the Nature and Stability of Alkene Cracking Intermediates in H-ZSM-5. *J. Catal.* **2017**, *345*, 53−69.
(109) Abbot, J.; Wojciechowski, B. W. The Mechanism of Catalytic Cracking of n -Alkenes on ZSM-5 Zeolite. *Can. J. Chem. Eng.* **1985**, *63*, 462−469.
(110) Buchanan, J. S. Reactions of Model Compounds over Steamed ZSM-5 at Simulated FCC Reaction Conditions. *Appl. Catal.* **1991**, *74*, 83−94.
(111) Sarazen, M. L.; Iglesia, E. Stability of Bound Species during Alkene Reactions on Solid Acids. *Proc. Natl. Acad. Sci. U. S. A.* **2017**, *114*, E3900−E3908.

https://doi.org/10.1021/acscatal.2c03360
ACS Catal. 2023, 13, 99−112